Multi-point temperature sensing in gas turbines using fiber-based intrinsic Fabry-Perot interferometers

Tyler Shillig

Thesis submitted to the faculty of the Virginia Polytechnic Institute and State University
in partial fulfillment of the requirements for the degree of

Master of Science
In
Electrical Engineering

Anbo Wang, Committee Chair
Gary Pickrell
Yong Xu

May 7th, 2012
Blacksburg, VA

Keywords: Optical Fiber Sensor, IFPI, Intrinsic Fabry-Perot Interferometer, Gas Turbine, Multi-point Sensing, Fiber-optic

Multi-point temperature sensing in gas turbines using fiber-based intrinsic Fabry-Perot interferometers

Tyler Shillig

ABSTRACT

Due to their compact size, sensitivity, and ability to be multiplexed, intrinsic Fabry-Perot interferometers (IFPIs) are excellent candidates for almost any multi-point temperature or strain application, and it is well-known that using a single-mode lead-in fiber, a multi-mode fiber section as the Fabry-Perot cavity, and an additional single-mode fiber as the tail results in a structure that generates strong interference fringes while remaining robust. Though the basic principles behind these sensors are understood, to the best of the author's knowledge there hasn't been a thorough investigation into the design and fabrication of a chain of multiplexed IFPI sensors for industrial use in an environment where serious issues associated with the size of the test coupon, sensor placement, and mechanical reinforcement of the fiber could arise. This thesis details the preparation and results of this investigation. It turns out that fabricating a sensor chain with appropriate sensor spacing and excellent temperature response characteristics proved a significant challenge, and issues addressed include inter-sensor interference, high-temperature mechanical reinforcement for bare fiber sections, and high bending losses. After overcoming these problems, a final sensor chain was fabricated and characterized. This chain was then subjected to a battery of tests at the National Energy Technology Laboratory (NETL), where four multiplexed sensors were installed on a 2"x2" coupon in a simulated gas turbine environment. Final results are presented and analyzed. The work that went into developing this chain lays the foundation for future efforts in developing quasi-distributed temperature sensors by identifying potential obstacles and fundamental limitations for certain approaches.

Dedications

I would be remiss if I didn't first and foremost thank God for giving me the opportunities and abilities He has given me throughout my life.

I am also eternally grateful for my family and close friends who provided a support network and pulled me through when times were hard and cheered with me when things went well.

I would also like to express my gratitude to the other members of our team that worked on this project: Cheng Ma, Di Hu, and Zhipeng Tian. When it was crunch time, we were beasts and met deadlines, no matter how daunting the obstacles. It was a pleasure to work with you guys.

I also truly appreciate my lab mates for your friendship and patience. Evan Lally, Jiajun Wang, Bo Dong, Dorothy Wang, Kathy Wang, and Cheng Ma were fantastic mentors, and I am forever indebted to you for your leadership and guidance.

Finally, I would like to thank Dr. Wang for fostering an environment of scholarship and excellence at the Center for Photonics Technology. Through the many years spent there, I have grown to love and respect the lab even more than when I first joined as an enthusiastic undergraduate.

Thank you all.

Acknowledgements

This work was fully sponsored by the Department of Energy's National Energy Technology Laboratory in Morgantown, West Virginia. Their financial support and enthusiasm for the work was appreciated immensely. The Department of Energy project number that corresponded to this work was DE-NT0005591.

Table of Contents

Listing of Figures

Listing of Tables

1 INTRODUCTION

1.1 Overview of Optical Fiber Sensors

The field of fiber optic sensing really began to take off in the late 1970s and early 1980s [1,2]. Enabled by the invention of the first laser in 1960 and the first true low-loss optical fiber in 1970, researchers discovered numerous applications for optical fiber sensors including, acoustic, magnetic, temperature, strain, and acceleration sensors using a variety of techniques [3]. Some of the initial approaches involved interruption-based shutter devices, which relied on a mechanical device selectively blocking the optical path, systems with strain-sensitive birefringence, as well as other exotic schemes. As the field has matured, a few highly effective sensing technologies have emerged as legitimate options for use in industrial applications [4]. These include fiber-Bragg gratings, and intrinsic and extrinsic Fabry-Perot interferometers. Each of these approaches offers advantages and disadvantages.

Fiber-Bragg gratings operate on the principle of partial Fresnel reflection by a series of precisely spaced refractive index changes. These changes are generated by intense UV light which permanently alters the refractive index profile of the target fiber. The most common means of generating these devices is by shining light through a phase mask onto the side of a target fiber. The polymethacrylate coating of a standard fiber is transparent to the light, but the photosensitive germanium-doped (most common) core is affected [5,6]. Due to the germanium dopant in the core, the most common FBGs are limited to approximately 700^{o}C.

The FBG fabrication technique illustrates one of the major advantages of FBG-based sensors. Because the fiber coating remains intact throughout the entire process, the mechanical integrity of the fiber is never compromised. An additional benefit is that cumbersome reinforcement is unnecessary and the final structure is small and easily handled. In spite of these advantages, there are several issues with FBGs that limit their effectiveness in an industrial application.

In order to multiplex these sensors, one of two techniques is commonly used: either making gratings which have peak reflectivity at different wavelengths (wavelength division multiplexing, or WDM), or by interrogating identical sensors with pulsed light and measuring the reflected signal from each sensor in the time domain, with slower return pulses representing more distant sensors (time-division multiplexing, or TDM). Both of these techniques allow for massively-multiplexed systems. However, the primary issue with the first technique is that the equipment required to fabricate the gratings is expensive, bulky, and complex, which is a major concern for industry partners. The second technique places limitations on the minimum inter-sensor spacing distance based on the temporal resolution of the detector being used [6]. Because of these advantages and disadvantages, FBGs are commonly used in applications like infrastructure monitoring where temperature or strain need to be measured at many locations over long distances, thereby reducing the per-sensor cost.

A second commonly used sensing technique is the extrinsic Fabry-Perot interferometer (EFPI). For additional information on Fabry-Perot interferometers, please refer to section 1.3. For now, a brief discussion of the general structure of the EFPI should suffice. These sensors use an air gap

between two fibers. As this cavity increases or decreases in length, an interference spectrum is generated, and a measurable signal is obtained. This geometry is attractive due to its simplicity, but also because non-standard fiber can be used as the waveguide. For ultra-high temperature sensing, these fibers may be sapphire or pure fused silica which allow a measurement range much higher than that offered by standard single-mode fiber which undergoes dopant diffusion at temperatures above ~800^{o}C [9,10].

In spite of this major advantage, because an external alignment housing is required to align and maintain the air gap between fibers, EFPIs tend to be bulky and fragile. Additionally, due to the strong reflection at each fiber/air interface and the high loss when coupling from the air gap back into the fiber, the number of sensors that can be multiplexed is very limited [11]. Due to these limitations, EFPI sensors are most commonly applicable to sensing in truly extreme environments like jet engines. An additional area where these are commonly used is in a situation where measuring a very large strain is required.

The optical fiber sensing technology to be discussed in this thesis is the intrinsic Fabry-Perot interferometer (IFPI). Like the EFPI, this technique relies on the interference fringes generated by reflections from two interfaces (see section 1.3). However, rather than using an air-filled gap, IFPIs utilize a section of another fiber with a slightly different refractive index. Because the refractive indices match so closely, the magnitude of the signal reflected at each interface is very small. Additionally, by carefully selecting the cavity fiber length and type it is possible to further reduce each individual sensor's loss to less than .5dB., allowing for numerous sensors to be multiplexed, although still much fewer than FBG-based systems [15,16]. Like FBGs the maximum temperature for standard IFPI sensors is around 700^{o}C due to dopant diffusion in the optical fibers. Also like FBGs, because the cavity of an IFPI sensor is simply another fiber, the overall footprint of the sensor is minimized. However, one drawback is that in their fabrication the fiber coating must be removed, which compromises mechanical integrity. However, the fabrication process is also an advantage that IFPI sensors have over FBGs due to the fact that inexpensive and common fiber optic equipment can be used. Additionally, at the beginning of this project, it was believed that there were no constraints on the inter-sensor spacing distance of IFPIs. It turns out that there is a minimum spacing distance, but this is much less than the minimum inter-sensor distance for FBGs being interrogated with time-domain multiplexing. See section 3.2 for a brief discussion of this issue. Table 1.1 below summarizes the advantages and disadvantages of each common sensor technology.

Table 1.1 - Summary of common optical fiber sensing technologies

	Advantages	Disadvantages
FBG	-Small footprint -Robust -Can be massively multiplexed	-Expensive fabrication -Expensive, complex interrogation (WDM) -Inter-sensor spacing constraints (TDM)
EFPI	-Extreme temperatures/strains possible	-Bulky -Fragile

		-Only a few can be multiplexed (<5)
IFPI	-Small footprint -Cheap, easy fabrication -up to ~15 can be multiplexed -no inter-sensor spacing issues* (see section 3.2)	-Less robust than FBGs -Not as many can be multiplexed as FBGs

1.2 Project Motivation and Constraints

As mentioned in the previous section, due to their compact size, sensitivity, and ability to be multiplexed, IFPI sensors are excellent candidates for many multipoint temperature or strain applications that require measurement at fewer than ten to fifteen locations. They are especially well-suited for industrial applications due to their cost-effective nature. However, geometric constraints resulting from the size of the test coupon and sensor placement requirements, can make fabricating a sensor chain with appropriate sensor spacing and excellent temperature response characteristics a significant challenge. Areas of investigation include inter-sensor interference, high-temperature mechanical reinforcement for bare fiber sections, and high bending losses. The primary merit of this work was overcoming these issues and delivering a robust product for a field test at the National Energy Technology Laboratory (NETL) at the US Department of Energy (DOE) in Morgantown, West Virginia. On November 16th, 2011, a chain of Fabry-Perot interferometric (IFPI) sensors fabricated in-house was subjected to a battery of tests. Subsequent chapters detail the design considerations necessary when fabricating IFPI sensor chains, as well as the final results of the field test. This engineering effort lays the foundation for future work in developing quasi-distributed temperature sensors by identifying potential obstacles and fundamental limitations for certain approaches.

The small-scale combustion chamber at the National Energy Technology Laboratory is designed to simulate the operating conditions found in gas turbines. Adjusting environmental variables and measuring their effect on temperature, burn efficiency, and chemical byproducts is the primary focus of this rig. As these complex processes are optimized, the improvements are incorporated into industrial power generation units, potentially resulting in higher efficiency, lower emissions, and in the end, lower operating costs. A variable that significantly affects combustion is the flow of cooling air downstream from the flame. One approach to understanding the impact of flow direction and magnitude on the overall process is measuring the two-dimensional temperature gradients across the coupon used to inject air into the system. The coupon measures 2” x 2” and is secured at the bottom of a tube, as shown at the very left-hand side of Figure 1.1. The inner square represents the bottom of the coupon. The sensors are installed on the top.

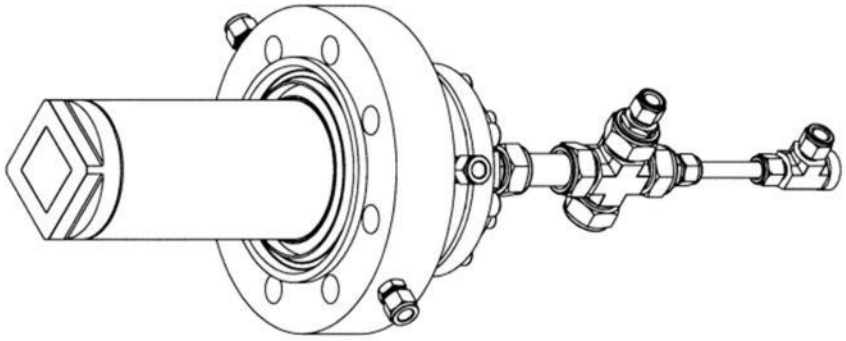

Figure 1.1 - Drawing of the cooling air injection setup (courtesy of the NETL)

It was determined that the temperature should be measured at four distinct locations on this coupon while pressurized high-velocity cooling air flowed through the coupon and the combustion chamber was subjected to a battery of tests. The initial design for the sensor layout as well as the coupon geometry is shown in Figure 1.2. In many ways the geometrical constraints provided an ideal test bed for addressing the above-mentioned weaknesses associated with optical fibers: the high-velocity air challenged the mechanical robustness and the coupon dimensions inherently required sharp bending.

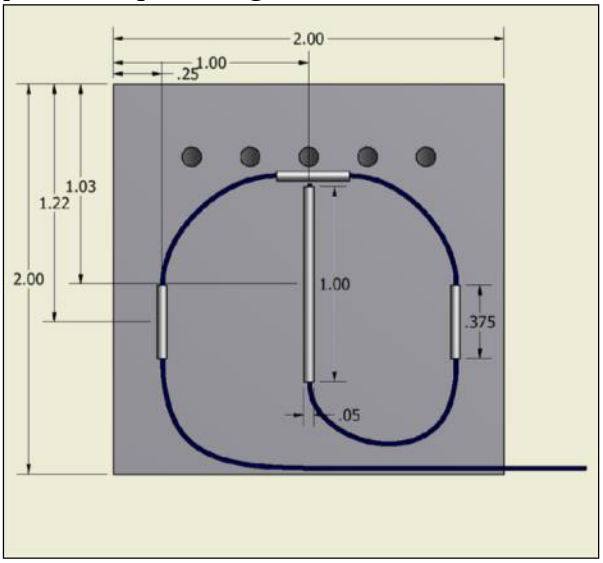

Figure 1.2 – Base coupon geometry with dimensions

1.3 Fundamentals of Fiber-Based Intrinsic Fabry-Perot Interferometers

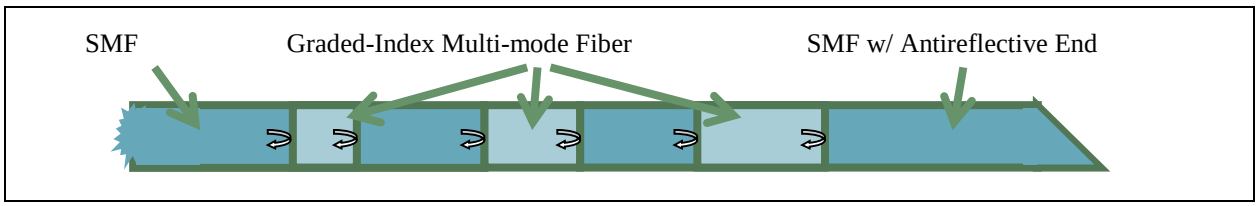

Figure 1.3 - Structure of Multiplexed Intrinsic Fabry-Perot Interferometers

Fresnel's equations (eq. 1, 2) describe the way that light is reflected at the interface between materials with two different refractive indices. θ_i and θ_t refer to the angle the incident light makes with the interface and the angle of the light with the interface after being refracted respectively.

$$r_{\parallel} = \frac{n_1 \cos(\theta_i) - n_2 \cos(\theta_t)}{n_1 \cos(\theta_i) + n_2 \cos(\theta_t)}, for\ field\ parallel\ to\ plane\ of\ incidence \quad (1)$$

$$r_{\perp} = \frac{n_1 \cos(\theta_t) - n_2 \cos(\theta_i)}{n_1 \cos(\theta_i) + n_2 \cos(\theta_t)}, for\ field\ perpendicular\ to\ plane\ of\ incidence \quad (2)$$

For the structure shown in Figure 1.3, we assume that the incident and transmitted angles equal zero, and therefore both equations simplify to

$$r = \frac{n_1 - n_2}{n_1 + n_2} \quad (3)$$

$$R = r^2 \quad (4)$$

where n_1 and n_2 correspond to the effective refractive index of either the single-mode fiber or multi-mode fiber.

The reflected light from the first and second interfaces of each individual sensor cavity (the MMF sections) interferes and generates an interference pattern described by eq. 5 [7].

$$I_r = I_i \cdot \frac{4Rsin^2\left(\frac{4\pi n_{eff} l}{\lambda}\right)}{(1-R)^2 + 4Rsin^2(\frac{4\pi n_{eff} l}{\lambda})} \quad (5)$$

A quick glance at this equation reveals that the intensity of the reflected signal is dependent upon the wavelength of light entering the cavity, as well as the difference in refractive index at the interfaces. As the wavelength of light entering the cavity shifts, the intensity varies sinusoidally with an overall magnitude governed by the difference in refractive index.

Throughout the design process, a variety of fibers were used with varying degrees of success. These will be discussed in the next section. For the final chain, SMF28 was used for the lead-in and inter-sensor fibers while GIF62.5/125 was used for the multi-mode fiber cavities. Figure 1.4 shows a prototypical interference spectrum generated by a single 1040um cavity. When several sensors are multiplexed, the spectrum retains its generally sinusoidal nature but has an envelope that is modulated by the other sensors in the chain.

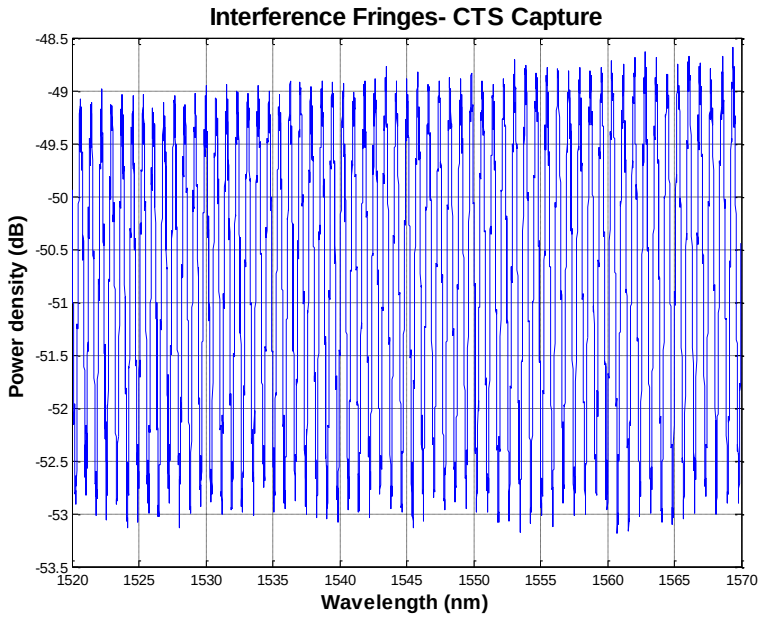

Figure 1.4 - Sample interference fringes from IFPI sensor with 1040um MMF cavity

2 BASIC DESIGN CONSIDERATIONS

2.1 Cavity Length

Sensor cavity length is one consideration that needed to be taken into account when designing a chain of IFPI sensors for use in a quasi-distributed sensing application. In order for the sensor to be demodulated accurately, the signal to noise ratio (SNR) should be maximized. Because the round-trip loss for the sensors at the beginning of the chain directly impacts the SNR of subsequent sensors, this loss should be minimized. Cheng Ma et. al. analyzed IFPI sensors with graded-index multi-mode fiber (GI-MMF) cavities and determined the relationship between total round-trip loss and length for 62.5/125um GI-MMF cavities, as shown in Fig. 2.1

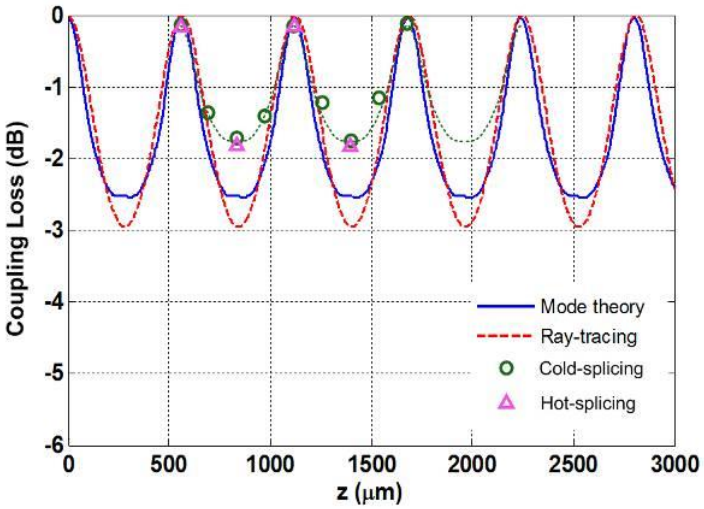

Figure 2.1 - IFPI Sensor Round-trip Loss vs. Cavity Length –Courtesy of Cheng Ma (1)

This sinusoidal loss behavior is due to the self-refocusing pitch length of the GI-MMF. Points that correspond to low loss represent positions where the mode field diameter inside the fiber is at a minimum, which provides ideal launching conditions for coupling back into a SMF fiber. For our application where only four sensors needed to be multiplexed, we selected cavity lengths of 520um, 1040um, 1560um, and 2080um. At these lengths, with optimized splice conditions which are highly dependent upon the specific model of splicer being used, we were able to achieve round-trip losses of between -.5dB and -.75dB for each sensor.

2.2 Lead-in Fiber Selection

In the initial stages of the project, one major point of concern was the losses induced in SMF 28 when subjected to the small bending radii required when mounting the fiber to the coupon. To address this, the bending performance of both SMF28 and a bend-insensitive fiber from Newport Optics was characterized. A test fiber was wound a single time around mandrels of varying sizes and a snapshot of the resulting spectrum (fig. 2.2, 2.3) was captured via CTS, Micron Optics model Si720.

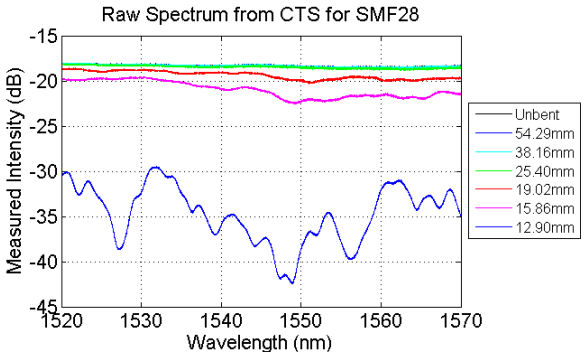

Figure 2.2 - SMF28 Spectra

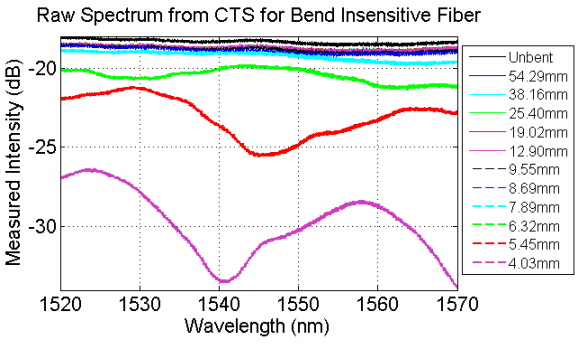

Figure 2.3 - Bend Insensitive Fiber Spectra

The bend-insensitive fiber has performance that is much better than the SMF28, but one new point of concern was the wavelength dependent loss. The signal demodulation algorithm for the IFPI sensors takes an FFT of the interference spectrum and then uses an FIR filter to eliminate the DC component of the signal. It can be seen that as the fiber loss increases, the loss over the entire spectrum is not equal, resulting in non-DC signal components from sources outside of the IFPI sensor. If these frequency components pass through the filter, the true signal from the sensor could be modulated by the bent fiber. To address this issue, the spectra for both SMF28 and bend-insensitive fiber at each bend diameter were processed using the signal demodulation algorithm (fig. 2.4, 2.5).

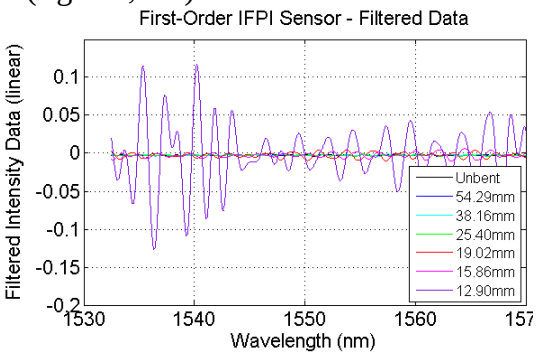

Figure 2.4 - SMF28 Pass-through Noise

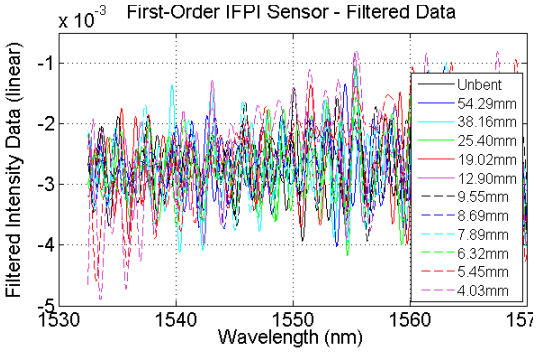

Figure 2.5 - Bend-Insensitive Fiber Pass-through Noise

At small bend diameters, it can be seen that the SMF28 loss spectrum has frequency components that pass through the filter, which would result in a distorted sensor signal. On the other hand, the FIR filter almost completely eliminates the noise associated with the bend-insensitive fiber, even when the bend diameter is very small. Figures 2.6 and 2.7 summarize the bending loss and noise findings respectively.

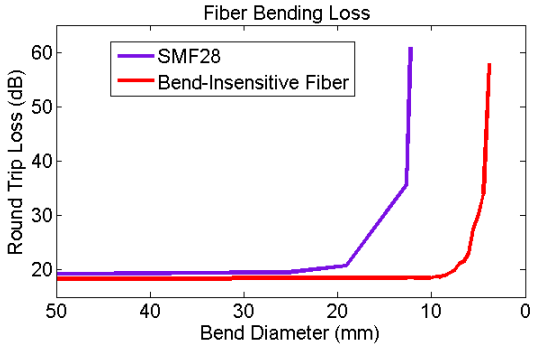

Figure 2.6 - Fiber Loss vs. Bend Diameter

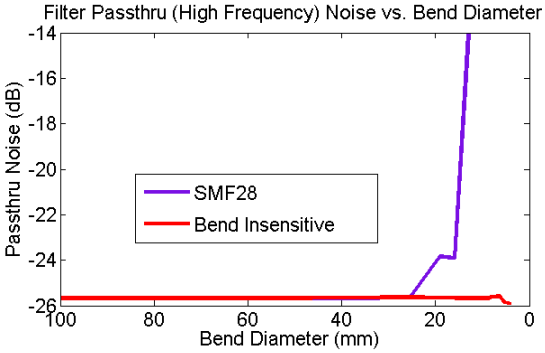

Figure 2.7 - Filter Pass-through Noise Magnitude

Because the bending performance of the SMF28 was marginal for the application, in the early stages of the project bend-insensitive fibers were exclusively used. However, due to issues such as weak splices and low signal-to-noise ratio (SNR), these were abandoned for SMF28 due to its combination of strong splices and excellent fringe visibility. A summary of the different single-mode fiber combinations that were used in conjunction with GI-MMF62.5/125 can be found in Table 2.1.

Table 2.1 - Summary of single mode fibers used in the fabrication of IFPI sensors

Fiber Type	Benefits	Drawbacks
F-SBC (Newport)	-After sensor fab, high success rate -Bending Performance	-Weak splices -VERY time consuming due to poor repeatability
ClearCurve (Corning)	-Bending performance -Sensors easy to fabricate	-Very weak splices -'bubbling' splices result in low repeatability for sensor fabrication
SMF28 (Corning)	-Strong splices -Clean signal -Easy fabrication	Marginal bending performance

3 SENSOR CHAIN DESIGN FOR USE AT THE NETL

Finalizing the sensor spacing and chain routing was one of the major challenges associated with this project. As shown in figure 1.2, the initial plan was to space each sensor approximately 3.2 cm apart from the others in a simple spiral shape, with the fiber surrounded by a stainless steel sheath and held to the surface of the coupon by four welded tubes. In order to fabricate the sensors, a section of bare fiber is necessary, and the original concept was to decoat an entire length of standard polymethacrylate fiber and then recoat the entire chain with a high-temperature polyimide coating and then insert this fiber into the stainless capillary tube before routing it through the hold-down tubes.

This approach failed for numerous reasons. First and foremost, the sensors were located too closely together, which seriously affected the signal quality. Additionally, the stainless steel tubing was extremely abrasive on the fiber, and when this was combined with a less-than-ideal polyimide coating, repeated breakages were the result. We carried out extensive studies of recoating the fiber for mechanical reinforcement, as will be discussed below.

3.1 Fiber recoating

The fiber recoating setup is shown in Figure 3.1(a), which comprises three parts: a glass chamber containing the polyimide solution, a tube furnace (for wet polymer drying), and a thin glass tube for aligning the wet fiber along the furnace axis to avoid touching the wall. The three pieces are aligned vertically. The long-term bending performance of the polyimide-coated fibers was tested at 350^{o}C. Due to the effort required to fabricate a single test piece, a large sample size was not feasible, but 15 coated fibers were fixed at a 1.9cm bend radius—the minimum bend radius

experienced by a fiber when installed on the coupon—and placed into a furnace. The survival rate after one week was over 80%. The performance of the coating can be further improved by increasing the thickness and uniformity of the coating, and a pursuing of achieving optimized performance is underway.

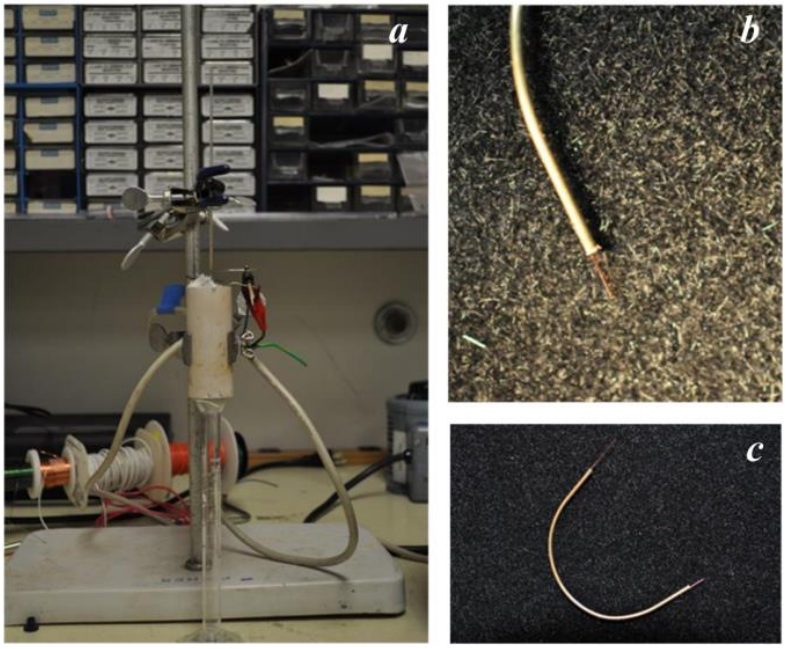

Figure 3.1 – (a) Fiber coating apparatus and the testing of the bending of the coated fiber (b) Nonuniform polyimide coating (lower-right) and commercial acylate coated fiber (upper-left). (c) The whole piece was curled to a radius of 0.75" and heated for 72 hours.

Although initial results were quite promising, perfecting the fiber coating process was much trickier than anticipated, and the initial study didn't accurately model the actual conditions that would be experienced by the final coated fiber. Although 1.9cm was the minimum bending radius, the failure rate of 20% over each individual short 4cm segment was unacceptable, because this indicated a much higher chance of failure at some point along a longer section of fiber. The primary issue was coating uniformity. The polyimide tended to coagulate rather than adhere uniformly to the fiber, which resulted in areas of nonuniform thickness that acted as stress concentrators. When the fiber was bent sharply, the non-uniform locations would inevitably snap. It was also postulated that micro-cracks in the glass due to the decoating process could be responsible for the breakage, but breakages occurred even when acetone was used to remove the polymer coating from the fiber.

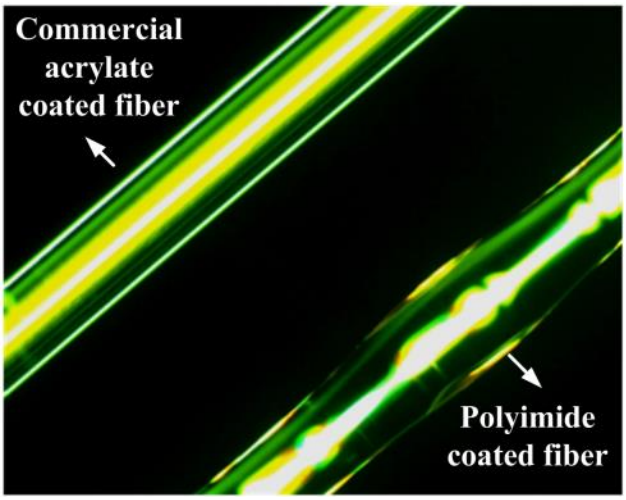

Figure 3.2 - Nonuniform polyimide coating (lower-right) and commercial acylate coated fiber (upper-left).

Significant effort was put into developing a more sophisticated coating process, but nonuniformities still cropped up occasionally, as shown in Figure 3.2. These nonuniformities compromised the repeatability of the work. When this issue was coupled with an update from the sponsor that temperatures in the combustion chamber were higher than initially anticipated, the fiber recoating process was dropped entirely in favor of gold-coated fiber. A summary of the materials used and resultant coating quality is found in Table 3.1. With additional work to eliminate nonuniformities, the PI-2525 from HD Microsystems should be an excellent fiber coating for applications requiring temperatures up to 400^{o}C. Recoating fibers requires a significant investment of time into both developing a sophisticated setup and optimizing coating conditions.

Table 3.1- Fiber coating materials and coating quality.

Product	MFG	Type	Results
HP1632	Michelman	Water-based polyimide	-Viscosity very low, requiring ~30 layers, and coating is brittle.
HP1432	Michelman	Water-based polyimide	-Higher viscosity, but coating remains brittle
PA845	Michelman	Water-based nylon solution	-Borderline temperature performance. -Good mechanical reinforcement
PZ33	Polyazeridine	Cross-linker for improving flexibility of Michelman	-No obvious results.
PI-2525	**HD Microsystems**	**Polyimide**	**-Excellent. Industry Standard.** **-Coating feels strong w/o brittleness.**

3.2 Gold-coated fiber

After dropping the initially proposed configuration, all subsequent designs relied upon gold-coated fiber with short sections of bare fiber corresponding to each sensor. These bare fiber sections were protected by sections of commercial polyimide-coated glass capillary tubing. This approach eliminated the issues associated with recoating and the stainless steel sheath, but the problem of determining the appropriate inter-sensor spacing remained, as well as the challenge of securing the extensive amount of additional fiber to the coupon in such a limited space. After some analysis and experimentation, it was determined that spacing the sensors approximately 15cm apart provided a the best signal quality by balancing the inter-sensor noise issue associated with short spacing with the increased bending losses associated with longer distances between sensors.

This balance proved very successful from a signal quality standpoint, and the additional fiber was initially just routed through the original hold-down tubing. However, during simulated environmental testing, it was found that the fibers rubbed against the edge of the hold-down tubes and breakages resulted. As a result, the free-form routing approach was adopted, and this proved very successful both in the lab and the field-test environment. All of these approaches are summarized with relevant photos in Table 3.2 found on the next page.

3.3 Summary of Routing Configurations

We have adopted four sensor chain configurations throughout the project. We started with the configuration shown in the inset figure I of table 3-2, in which a section of stainless-steel tubing with matched outer diameter with the inner diameter of the hold-down tubes was used to secure the sensing fiber. We originally designed this schematic expecting the best mechanical integrity provided by the metal tubing. However, as we demonstrated through designed experiments, the fiber zig-zagged inside the metal tubing to introduce highly localized strain, which consequently broke the fiber during installation. Even with the strong gold-coated fiber, breakage during installation was not avoidable, and as a result, this scheme was finally abandoned. Later we switched to the simple mounting scheme using gold coated fiber, shown in the inset figure 1 of table 3-2. Such geometry provides great flexibility during installation, and demonstrated great mechanical endurance.

However, a major issue was that the sensors have to be cascaded with very small spacing (~1") which generates significant cross-talk between adjacent sensors. To eliminate the cross-talk, we developed the "multi-wrap" scheme, labeled as scheme 2 in table 3-2. This scheme demonstrated the best performances in terms of mechanical strength and signal quality by then, but the sharp bending between the neighboring hold down tubes initiates the potential of fiber breakage at high temperature. We finally adopted the mounting scheme 3 in table 3-2. This scheme provides the best flexibility in sensor installation and robustness by eliminating sharp bending unavoidable in any of the former schemes.

Table 3.2 - Summary of routing configurations

Scheme number	Characteristics	Figure
Initial	**Initially Proposed Configuration** Benefits: Elegant**;** Stainless protective tubing is very robust**;** Good thermal transfer Issues: Interference between closely spaced sensors; Stainless tubing abrades fiber, resulting in breakages. Issue with antireflective end being too close to steel	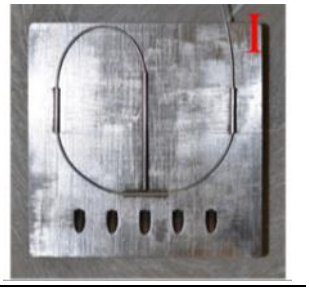
1	**Glass Capillary Tubes over Bare-Fiber Sections** Benefits: Installation is tricky but repeatable; Issues: Interference between closely spaced sensors; Sensor response is reduced due to insulating glass tubing; Issue with antireflective end being too close to steel	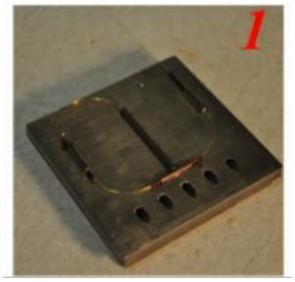
2	**Increased Inter-sensor Spacing** Benefits: Installation is simple; Long spacing resolves sensor crosstalk issue Issues: Higher bending losses due to the number of tight bends; Loops are difficult to control and are easily tangled.	
3	**Free-form Routing** Benefits: Minimizes regions of stress concentration near the edges of hold-down tubes, breakages much less frequent; Bending losses are reduced; less crosstalk. Issues: Complicates placement into test rig.	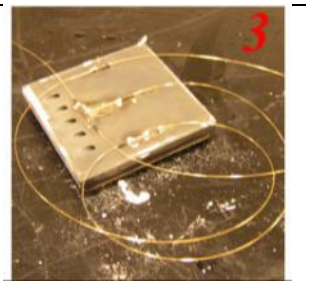

4 SENSOR AND CHAIN FABRICATION

4.1 Sensor fabrication

The major steps for the sensor fabrication using Au-coated fiber are summarized below, in table 4.1. The key component for the fabrication is a precision cleaver with a 1D translation stage. The stage and cleaver have their fiber axis aligned and their positions fixed. During fabrication, the IFPI cavity length can be easily controlled by adjusting the 1D stage after accurate alignment of the splicing point with respect to the cleaver's blade.

Table 4.1 - Sensor fabrication procedure.

Descriptions	Figures
Sensor Fabrication: 1) Strip ~2.5cm from Single Mode Fiber 2) Note the reflected signal strength at the CTS 3) Align polymer/stripped interface such that the bare fiber end will be ~7-10mm after cleaving 4) Strip ~4cm of MMF and splice onto the end of SMF. Break MMF right at the its polymer/stripped interface without removing SMF from the cleaver holder 5) Reinsert the fiber holder into the cleaver and using a stereo microscope confirm that the SMF→MMF splice is lined up with the cleaver blade. 6) Slide stopper block attached to micrometer up until it touches the end of the fiber holder. 7) Dial the stopper block back the desired distance 8) Slide fiber holder back until it touches the stopper 9) When the fiber is cleaved, the MMF section spliced to the end of the SMF should be almost exactly the desired length. 10) Note the reflected signal strength at the CTS a) The reflected signal strength should be at most 1-2db lower than the initial value b) The reflected signal should have a small (~.25db) sinusoidal component c) If both of these requirements aren't met, either the cleave or splice is bad and sensor should be remade 11) Cut fiber and set this 'half sensor' section aside for use in the chain construction Repeat for additional sensors	Steps 5-9+: Red circles indicate contact. 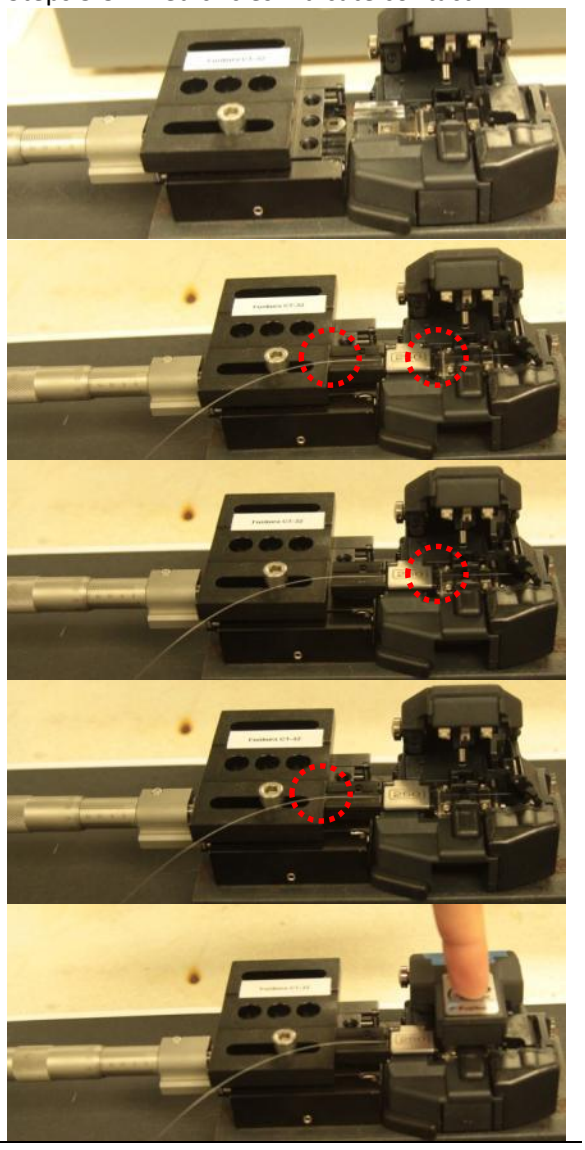

4.2 Chain fabrication

The chain fabrication process is summarized below (and illustrated in Figure 4.1):

1. With a half-sensor still attached to the SMF, strip ~2.5cm from the end of the next sensor to be located in the chain, cleave the end in such a way that there is a minimal amount of bare fiber remaining (same as step #1 above).
2. Splice the SMF portion of the half-sensor link onto the end of the MMF section of the half-sensor still attached to the CTS. This completes the first full sensor. Loop a small knot into the middle of the second half-sensor link to eliminate any reflection from the end of the fiber, and then capture the spectrum from the CTS. This spectrum represents the performance of the first sensor in the link
3. Repeat this process for the remaining half-sensor links
4. Fabricate an antireflective end by either 'junk cleaving' an SMF fiber in such a way that ~-60dB of loss is induced, or polish the end face at a 12^{o} angle for antireflection purposes while monitoring the loss
5. Splice this antireflective section onto the end of the chain.
6. Capture and characterize performance.

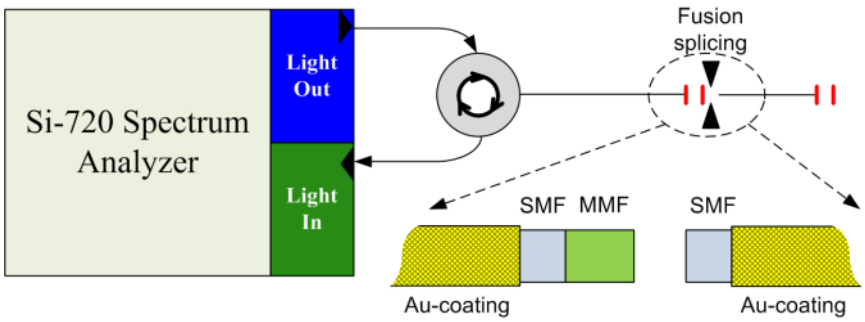

Figure 4.1 - Illustration of the sensor chain fabrication process. SMF: single-mode fiber; MMF: multi-mode fiber.

5 PERFORMANCE CHARACTERIZATION AND TESTING

5.1 Sensor Evaluation

Irrespective of the fiber used or inter-sensor spacing, the chains were characterized using the same technique and then compared with one another. Due to improvements in technique and process optimization, total time for fabricating a viable sensor chain was controlled to be within 2 hours. The spectrum of the fabricated chain was captured by a CTS. Both the wavelength domain and the wavenumber domain provide valuable insight into the performance of a given chain. Figure 5.1 shows the characteristics of a typical chain.

The peak-to-valley strength as well as sharpness of the spikes in the bottom two plots have a direct impact on the accuracy and demodulability of the sensors. Each spike in 5.1(c,d) represents a single sensor. Both plots represent the same chain, but the signal strength for sensors 2, 3, and 4 clearly falls off after installation due to bending losses.

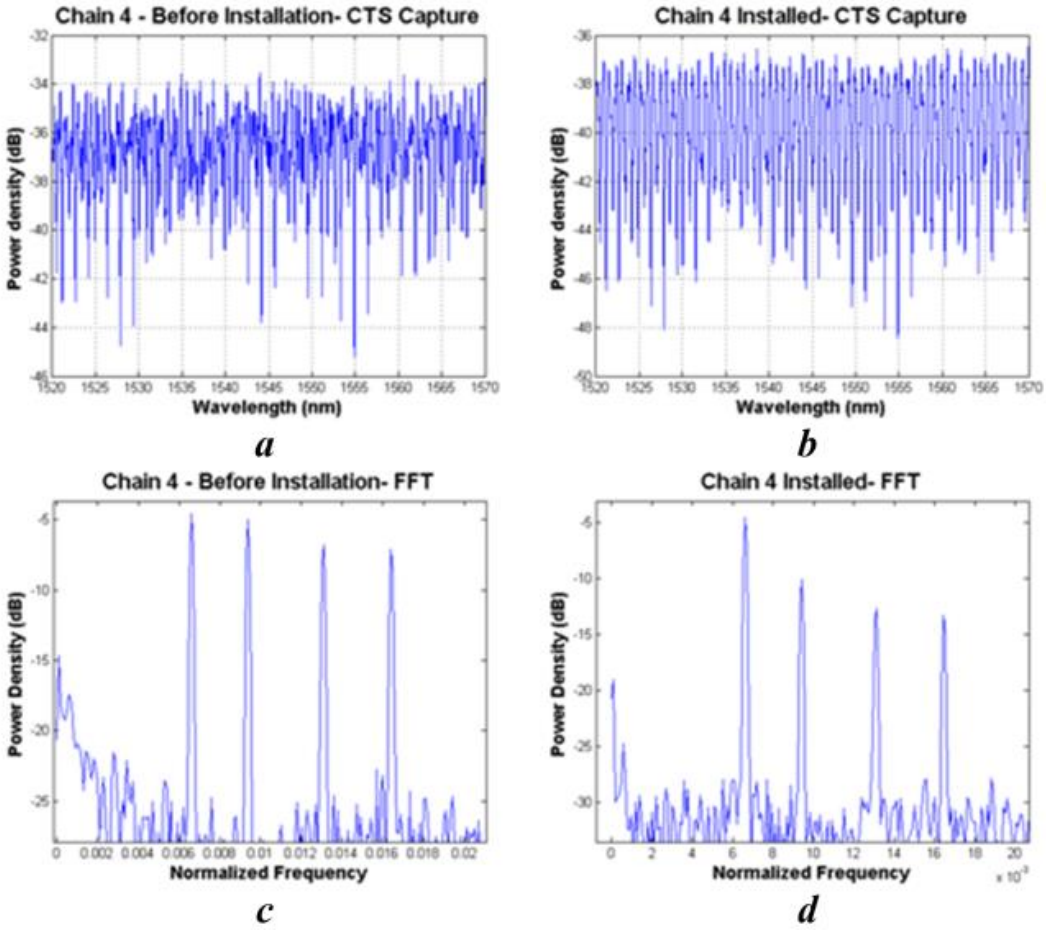

Figure 5.1 - Typical performance characteristics of a 4 sensor chain before and after installation

The upper two plots clearly show the roughly periodic nature of the spectrum, which is a superposition of frequencies corresponding to each of the sensors combined with any background noise. The 'purity' of each period in the sinusoid associated with each sensor can be quantified. The 'chirp', or deviation from a pure central frequency, is shown for each sensor in Figure 5.2, and has strong correlation with overall accuracy and sensitivity.

We found that the frequency impurity, as denoted by "chirp" of the spectrum, was an effective measure of the sensor's performance. Larger frequency chirp amounts to greater demodulation uncertainties, in turn, the sensor accuracy would sacrifice. Through extended experiments, we qualitatively confirmed the relationship between chirp intensity and sensor accuracy, which is the basis for using the chirp intensity as an evaluation standard upon which different sensor links were compared. It was discovered that the chirp was highly dependent on several factors, the most prominent among them being the sensor spacing. Experimental evidence positively supported a significant increasing tendency of the chirp with decreased sensor spacing. This was attributed to the crosstalk between neighboring sensors caused by non-vanishing cladding modes

that were coupled into downstream sensor cavities. When inter-sensor spacing is large, the excited cladding modes at the fiber splicing interface will experience significant attenuation by the time they reach the successive sensors, however the attenuation decreases when spacing between sensors is reduced.

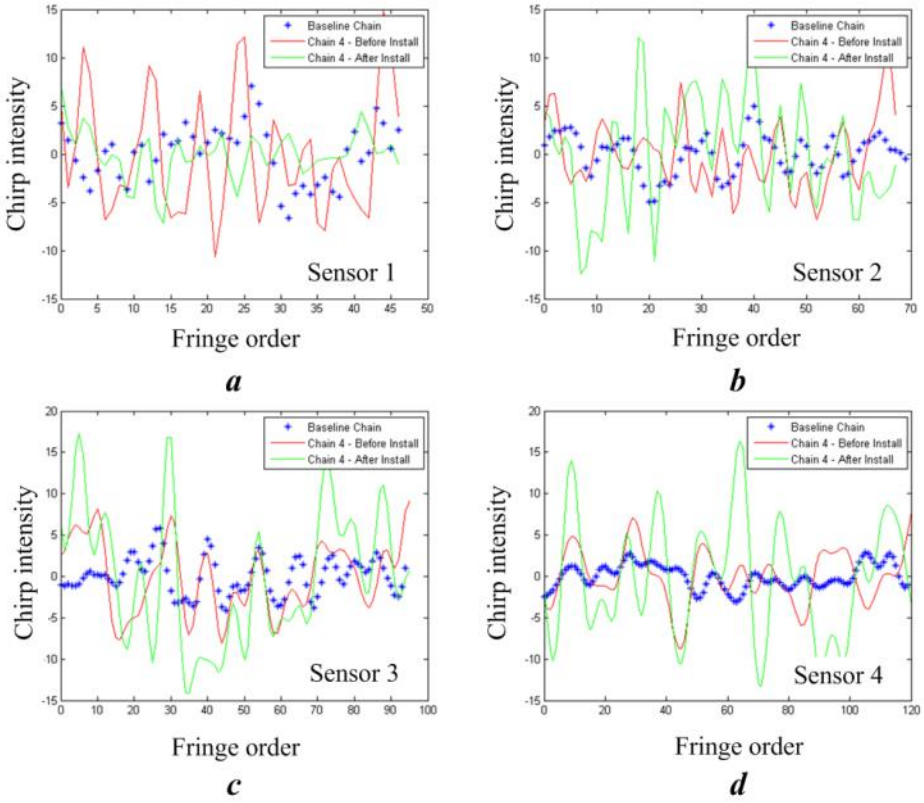

Figure 5.2 - Calculated chirp intensities of the sensors multiplexed in one link. The cavity lengths are (a) 1040 µm, (b) 1560 µm, (c) 2080 µm and (d) 2600µm. Colors represent different installation steps.

One important detail to note when analyzing these results is that the exact correlation between the chirp and sensor accuracy and sensitivity is unknown. As such, each sensor's performance must be compared to another sensor with proven performance. In figure 5.2, the installed chain shows a significantly increased chirp as compared to that before installation. This is attributed to two factors. 1) the loss associated with bending decreases the signal to noise ratio, which correspondingly increases the effective influence of random noise falling within the digital bandpass filter; 2) the bending of the fiber induces stronger cladding mode excitation, which contributes to the significant enhancement of the chirp. Plotted in the figure in blue color are the chirp curves from a "standard" chain with best performance, which was referred to as the "baseline chain". In our research, it was found that sensors with chirp values less than approximately 5 times that of the baseline chain performed well.

5.2 Sensor Calibration

After confirming that the sensor chain would exhibit satisfactory accuracy and sensitivity, the next step in the procedure was calibrating the chain to a known standard. This process essentially correlates the spectrum at a given temperature with a thermocouple reading. By repeating this process at a number of different points between room temperature and the maximum anticipated operating temperature, it is possible to anticipate the spectrum's behavior through a full range of temperatures. For the field test, where the maximum temperature was expected to be 600°C, the temperature was stabilized and sampled at around 35°C intervals, giving 15-20 data points. Fig. 5.3 shows a sample calibration curve for an ordinary sensor.

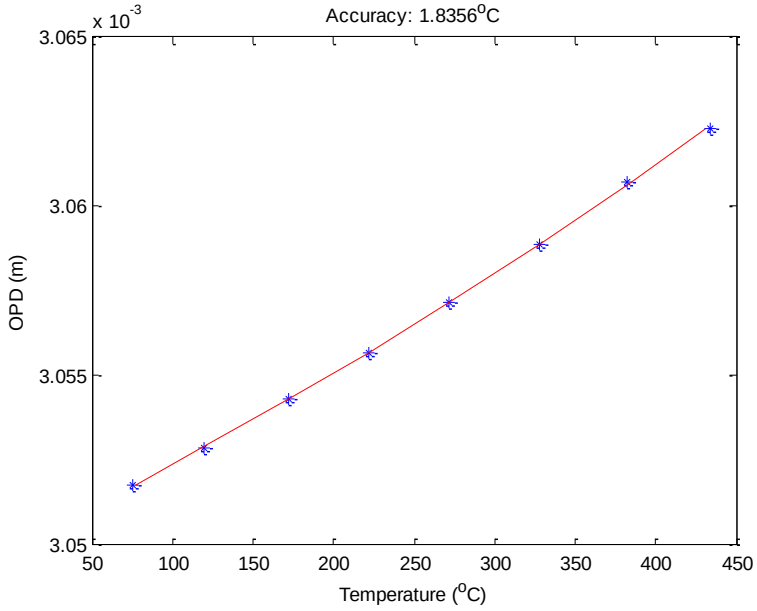

Figure 5.3 - Calibration curve for standard sensor showing relationship between temperature and OPD

5.3 Simulated Environmental Test

In order to confirm that the proposed design would survive the field-test environment, a chamber, shown in 5.4(a), was fabricated to simulate similar conditions. The coupon with a sensor chain installed sat inside the chamber in a furnace while the temperature was raised to 400°C. The chamber was then pressurized to 100psi and the cool air was forced through the holes in the coupon in a manner identical to the combustion chamber located at the NETL. This process is shown in 5.4(b), the dramatic decrease in the measured temperature was due to the injection of the cooling air. With the high speed air flow impinging on the coupon surface, the whole chain was subject to severe vibrations. Through the test, we confirmed the following: 1) the strong vibration of the sensor would not affect the signal quality and 2) the air flow would not induce potential breakage at 100psi. Subsequent tests were run at temperatures up to 650°C, at which point the aluminum chamber melted. However, it was confirmed that the sensor chains were robust and capable of withstanding high temperatures, while still producing accurate results.

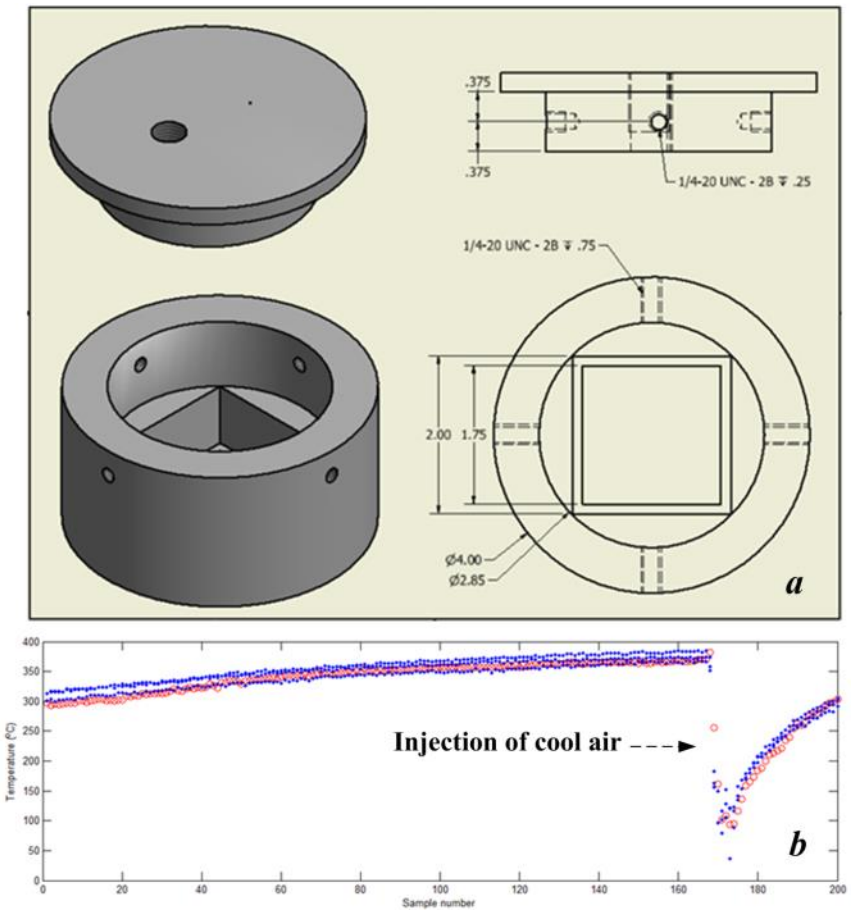

Figure 5.4 - (a) Mechanical drawing of the environmental test chamber design. (b) the measured temperature using an installed sensor chain during the testing process.

6 SENSOR INSTALLATION, TESTING, AND RESULTS

6.1 Design of the Assembly

The assembly required to attach the fiber feedthrough to the existing system was constructed according to dimensioned drawings provided by the NETL. Figure 6.1(a) shows the final assembly. The pressure-rated fiber feedthrough can be clearly seen on the right-hand-side of the assembly. The tubing provides working space for fiber splices. Due to concerns about high-velocity air and its impact on the survivability of the unprotected fiber inside the 1" tubing in the center, a perforated plug was installed into the left-most side of the tubing. The fiber was fed through the center hole in the plug, and the relatively tight tolerances served to minimize fiber vibration. The holes drilled around the circumference of the plug eliminate a pressure difference across the plug, which eliminated the danger associated with using an unrated and untested pressure boundary.

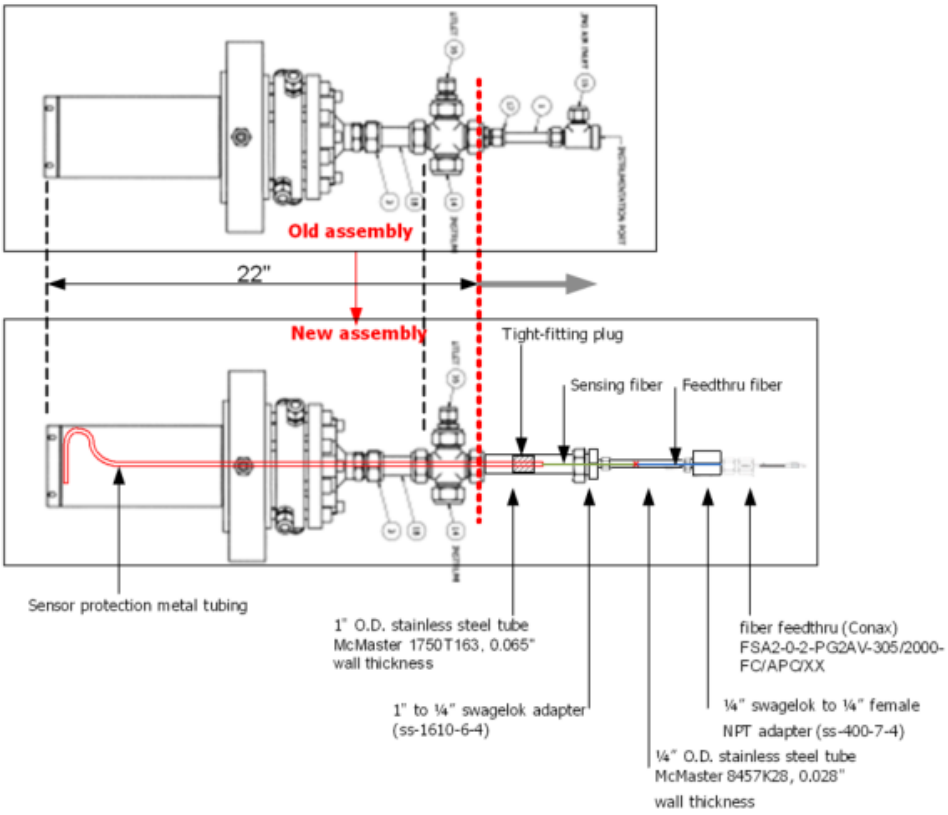

(a)

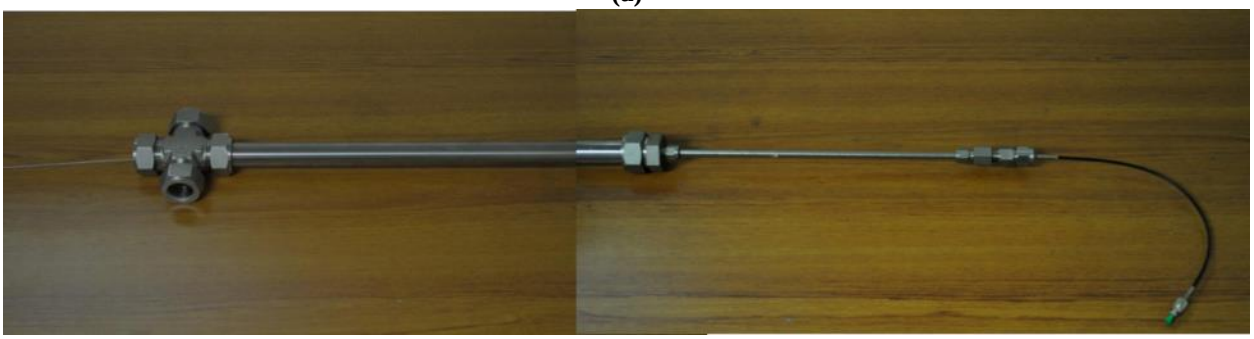

(b)

Figure 6.1 - (a) Design of the optical fiber feedthrough assembly. (b) Feedthrough assembled in the lab.

The metal plug was machined with the O.D. slightly larger than the I.D. of the 1" O.D. tubing. A central bore of the size slightly larger than the O.D. of the protection metal tubing was drilled for fiber stabilization. To install the plug into the outer tube, the tube was heated prior to insertion of the plug, to thermally expand its dimension. After heating, the plug was inserted into the outer tube, and fixed very firmly when the tube cooled down. The fiber intruding from the 1" tube and the fiber connected to the feedthrough (both fibers are with redundant lengths) were fusion spliced together after they were cut down to their desired length. The extra fiber was curled inside the 1" tube, and the larger tube was finally attached to the smaller tubing using a tubing adapter. Figure 6.2(a) illustrates the design for the plug, and its relative position with the fiber

and outer tubing. Figure 6.2(b) is a photograph showing the machined plug installed inside the 1" tube.

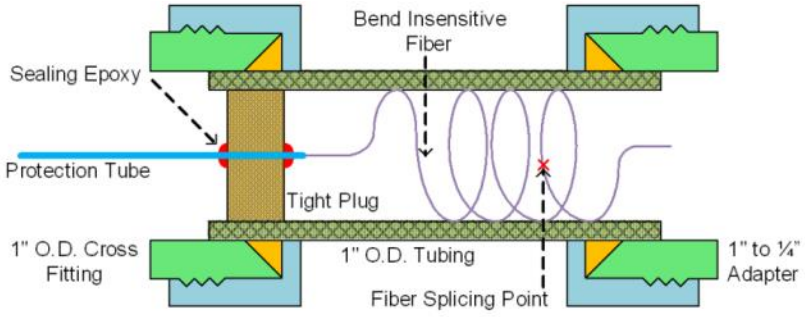

(a)

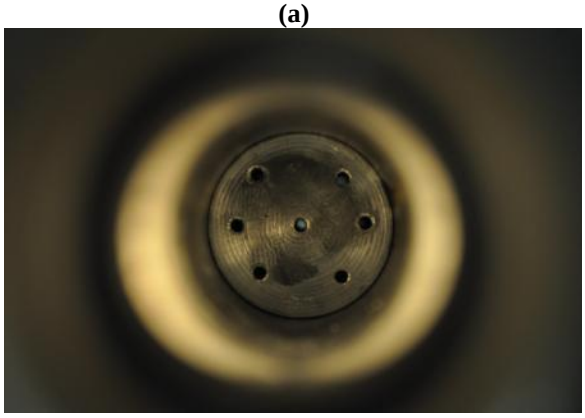

(b)

Figure 6.2 - (a) Design of the 1" O.D. tube with the fitting plug. The plug provides stabilization of the metal tubing, and the bend-insensitive fiber will be curled inside the tubing. (b) Cross-sectional view showing the machined plug. The central bore is for the fiber to go through, while the surrounding holes provide air-path to maintain balanced pressure on both sides of the plug.

6.2 Installation Procedure

Installing the entire setup into the existing system followed this procedure:

1. Insert fiber and sensor chain into a section of stainless steel microtubing for protection
2. Secure the microtubing in the first coupon holddown and then route the fiber through the remaining holddowns
3. Install the coupon and fiber sensors into the coupon holder provided by the NETL
4. Run the optical fiber and protective tube up through the existing chambers, through the anti-vibration plug, and then through the new tubing assembly until the end of the fiber passes completely through the .25" tubing which interfaces with the (disconnected) commercial fiber feedthrough
5. The stainless steel protective tubing will end ~3 cm to the right of the anti-vibration plug
6. Splice the end of the fiber with the fiber coming out of the commercial fiber feedthrough

7. Carefully attach the fiber feedthrough to the .25” tubing while coiling the excess fiber into the 1” tubing.
8. Tighten all fittings and test for leaks.

a. Field installation

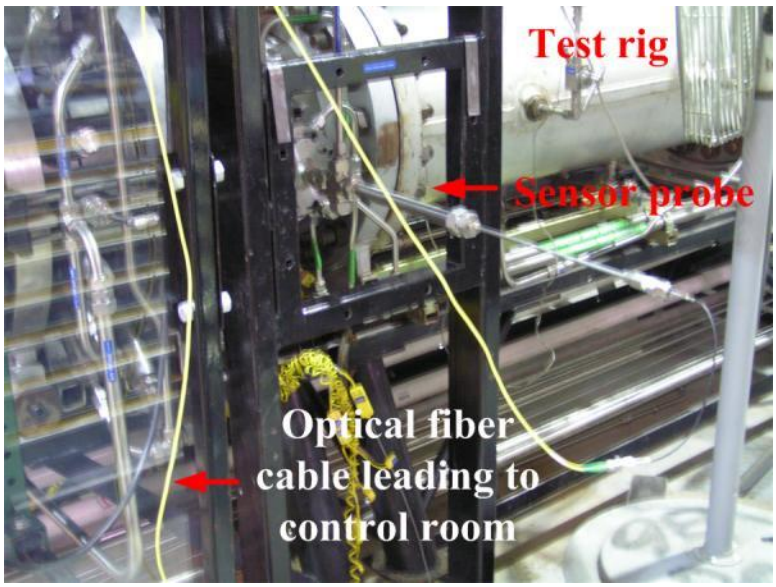

Figure 6.3 - Photo of the installed fiber optic probe (photo taken during the field test).

Upon arrival at the NETL on Nov. 15th, 2011, a sensor chain was installed in the system. This chain was routed in configuration 2, i.e. multiple loops routed through the hold-down tubes. Unfortunately, upon installation this chain broke, and was subsequently replaced with the final sensor chain. This chain was routed in configuration 3, i.e. free-form routing. The following morning this sensor chain was subjected to a battery of tests and harsh operating conditions, including temperatures up to 700ºC. The installed assembly is shown in figure 6.3

6.3 Field Test Results

The field test started at 9:30 a.m., November 16th, 2011. The test lasted for 5.5 hours, during which the maximum coupon temperature reached beyond 700ºC. The sensor signal was remotely interrogated with a 10-meter SMF28 (Corning Inc.) optical fiber cable, which was connected to the Component Testing System (Model Si-720, Micron Optics, Inc.), a scanning rate of 5 Hz (rather than 0.5Hz) was used to minimize the scanning-rate induced additional phase term in the spectrum. The spectral interrogation unit interfaced with a laptop through a General Purpose Interface Bus (GPIB) cable. Data acquisition and processing were performed with a Matlab based platform. Signal demodulation was performed in real-time using the direct OPD estimation algorithm. During the field test, the cooling air flow rate and the gas pressure in the rig were adjusted during different periods, giving rise to controlled temperature change on the coupon surface (See Table 6.1).

Table 6.1 - Parameters affecting the coupon temperature during the field test.

Parameter	Minimum	Maximum	Relationship with temperature
Rig pressure (psig)	1.54	30.48	Temperature increases with rig pressure
Cooling air flow rate (scfh)	48.85	400	Temperature decreases with cooling air flow rate
Total air flow rate ($\times 10^4$ scfh)	0.2982	3.3449	Temperature increases with total air flow rate

The real-time monitored temperatures measured by the sensors were co-plotted in figure 6.4. Post-processing was conducted by Cheng Ma. The relatively large noise depicted in the figure is due to the poor resolution associated with the direct OPD estimation algorithm. However, the measured raw temperature delivered some important information: 1) the temperature changes measured showed excellent agreement with the inner rig temperature measured with thermocouple 2) the sensors demonstrated the existence of a significant temperature gradient across the coupon. The sensor at the middle far from the air holes (black) showed the highest temperature, throughout the entire test. With cooling air, the sensor in the middle closest to the air holes (pink) had the lowest temperature, whereas the temperature measured by the sensors at two sides (blue and red) were the lowest when cooling air was turned off. The maximum temperature gradient was almost 100°C across the length from the middle to the edge of the coupon. This trend was in agreement with expectation and with the temperature map recorded by an optical pyrometer that imaged the bottom side of the coupon.

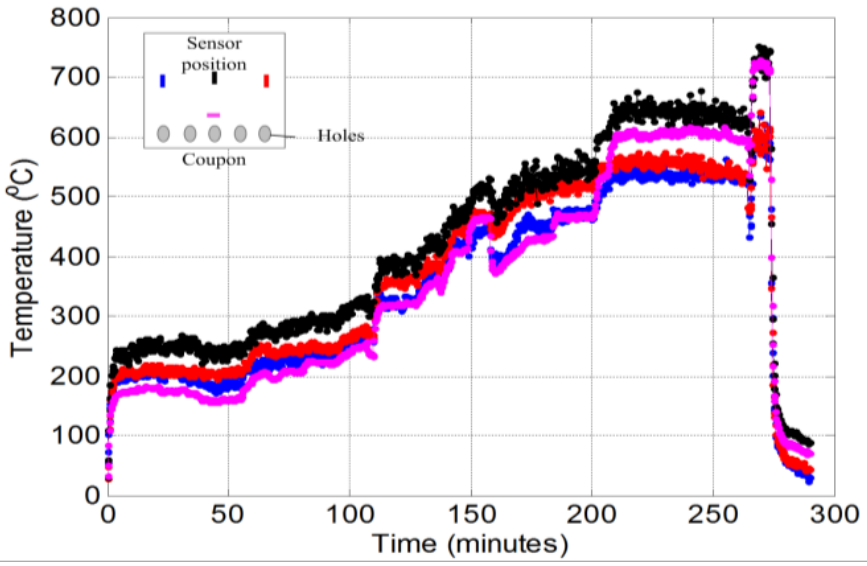

Figure 6.4 - Measured temperature (real time) using the direct OPD demodulation algorithm.

As depicted in figure 6.5 on the next page, using a sophisticated total phase algorithm results in significant noise reduction, which more clearly reveals the details of the temperature history. In the same figure, the measured values of the parameters listed in table 6.1 were co-plotted with the same time scale to better expose their correlations.

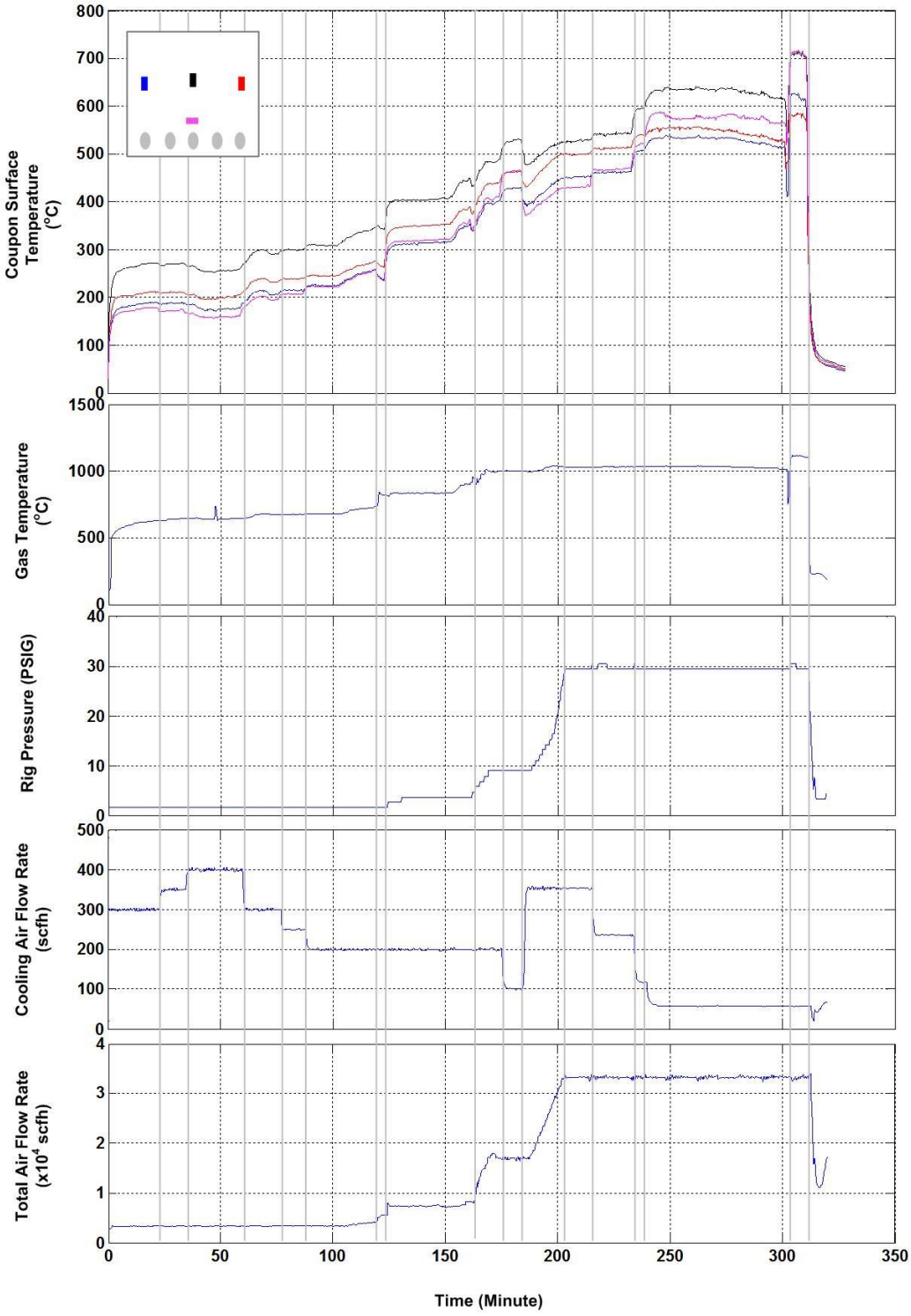

Figure 6.5 - Post-processed data with the total phase algorithm. The control parameters are plotted with the same time scale for better comparison.

7 CONCLUSION

In every respect, this project was an unqualified success, once again establishing the value of optical fiber sensors to the field of extreme environment sensing. Important findings from the research effort include:

1) A much more complete understanding of the interaction between multiplexed sensors and the impact of each sensor on the overall chain performance.
2) Familiarity with different fiber coatings for use in different circumstances
3) Improved IFPI fabrication techniques increase the overall consistency and quality of experiments
4) Understanding of the impact of bending loss and sensor spacing on signal demodulation

It is my sincere hope that this work and these findings will contribute to future research at the Center for Photonics Technology and the field of fiber optic sensing in general. For future projects with similar objectives, these findings should provide valuable direction throughout the design and fabrication process. Last but not least, this work was funded by the Department of Energy through the National Energy Technology Laboratory, and their support and enthusiasm was appreciated immensely.

REFERENCES

(1) W. Gopel, J. Hesse, J. N. Zemel, “Sensors, a comprehensive survey – Chapter 15: Optical-Fiber Sensors”, VCH Verlagsgesellschaft mbH, 1992

(2) J. Palais, “Fiber Optic Communications 4th ed.,” Prentice Hall, New Jersey, pp. vii-2, 1998

(3) G.D. Pitt, P. Extance, et. al., "Optical-fibre sensors," Optoelectronics, IEEE Proceedings J , vol.132, no.4, pp.214-248, August 1985

(4) Byoungho Lee, “Review of the present status of optical fiber sensors,” Optical Fiber Technology, Volume 9, Issue 2, April 2003, Pages 57-79

(5) A. Othonos, “Fiber Bragg Gratings”, Rev. Sci. Instrum. 68, 4309 (1997)

(6) C. Doyle, “Fiber Brage Grating Sensors: An introduction to Bragg gratings and interrogation techniques”, Smart Fibres, www.smartfibres.com, 2003

(7) K. Hill, G. Meltz, “Fiber Bragg Grating Technology Fundamentals and Overview”, Journal of Lightwave Technology, Vol 15, No. 8, (1997)

(8) A.D. Kersey, T.a. Berkoff, and W.W. Morey, “Multiplexed fiber Bragg grating strain-sensor system with a fiber Fabry—Perot wavelength filter”, Optics Letters, Vol. 18, Iss. 16, pp. 1370-1372 (1993)

(9) W. Liang, Y. Huang, Y. Xu, Highly sensitive fiber Bragg grating refractive index sensors Appl. Phys. Lett. 86, (2005)

(10) J. Wang, B. Dong, E. Lally, et. al., “Multiplexed high temperature sensing with sapphire fiber air gap-based extrinsic Fabry–Perot interferometers,” Optics Letters, vol. 35, Issue 5, pp. 619-621 (2010)

(11) K.A. Murphy, M.F. Gunther, et. al. “Optical Fiber Sensors”, Lasers and Electro-Optics Society Annual Meeting, 1995. 8th Annual Meeting Conference Proceedings, Volume 1., IEEE (Invited article)

(12) Z. Wang, “Intrinsic Fabry-Perot Interferometric Fiber Sensor Based on Ultra-Short Bragg Gratings for Quasi-Distributed Strain and Temperature Measurements”, Doctoral Dissertation, Virginia Tech, Blacksburg, VA, 2006.

(13) K. Hill, Y. Fujii, D. C. Johnson, and B. S. Kawasaki, “Photosensitivity in optical fiber waveguides: Application to reflection filter fabrication,” Appl. Phys. Lett., vol. 32, pp. 647–649, 1978.

(14) B. S. Kawasaki, K. O. Hill, D. C. Johnson, and Y. Fujii, “Narrow-band Bragg reflectors in optical fibers,” Opt. Lett., vol. 3, pp. 66–68, 1978.

(15) C. Ma, B. Dong, et. al. “Optimization of Single-/Multi-/Single-Mode Intrinsic Fabry-Perot Fiber Sensors”, Journal of Lightwave Technology, Accepted but not yet published

(16) C. Ma, E. M. Lally, and A. Wang, "Toward Eliminating Signal Demodulation Jumps in Optical Fiber Intrinsic Fabry-Perot Interferometric Sensors," Journal of Lightwave Technology, vol. 29, pp. 1913-1919, 2011.

(17) T. W. Kao and H. F. Taylor “High-sensitivity intrinsic fiber-optic Fabry—Perot pressure sensor“, Optics Letters, Vol. 21, Issue 8, pp. 615-6

(18) Z. Huang and Y. Zhu, “Intrinsic Fabry–Pérot Fiber Sensor for Temperature and Strain Measurements”, IEEE Photonics Technology Letters, Vol. 17, No. 11, Nov. 2005

(19) C. Ma and A. Wang, “Multimode excitation-induced phase shifts in intrinsic Fabry-Perot interferometric fiber sensor spectra”, Applied Optics, No. 49, Sep. 2010

(20) W.H. Tsai and C.J. Lin, “A Novel Structure for the Intrinsic Fabry–Perot Fiber-Optic Temperature Sensor”, Journal of Lightwave Technology, Vol. 19, No. 5, May 2001

(21) A. Yariv and P. Yeh, “Photonics: Optical Electronics in Modern Communications, 6th ed.”, pp160-170, Oxford University Press, 2007

(22) G. Fowles, ”Introduction to Modern Optics, 2nd ed.”, pp. 90-96, Dover Publications, New York 1989

(23) C.E. Lee, R.A. Atkins, and H.F. Taylor, “Performance of a fiber-optic temperature sensor from -200 to 1050^{o}C”, Optics Letters, Vol. 13, Issue 11, pp. 1038-1040 (1988)

(24) Q. Wang, G. Farrell, and W. Yan, "Investigation on Single-Mode-Multimode-Single-Mode Fiber Structure," J. Lightwave Technol., vol. 26, pp. 512-519, 2008.

(25) S. M. Tripathi, A. Kumar, R. K. Varshney, Y. B. P. Kumar, E. Marin, and J.-P. Meunier, "Strain and Temperature Sensing Characteristics of Single-Mode-Multimode-Single-Mode Structures," J. Lightwave Technol., vol. 27, pp. 2348-2356, 2009.

(26) Q. Shi, Z. Wang, L. Jin, Y. Li, H. Zhang, F. Lu, G. Kai, and X. Dong, "A Hollow-Core Photonic Crystal Fiber Cavity Based Multiplexed Fabry-Perot Interferometric Strain Sensor System," Photonics Technology Letters, IEEE, vol. 20, pp. 1329-1331, 2008.

(27) Z. Huang, Y. Zhu, X. Chen, and A. Wang, "Intrinsic Fabry-Perot fiber sensor for temperature and strain measurements," Photonics Technology Letters, IEEE, vol. 17, pp. 2403-2405, 2005.

(28) G. Yuan, G. Yu, R. Yun-Jiang, Z. Tian, and W. Yu, "Fiber-Optic Fabry-Perot Sensor Based on Periodic Focusing Effect of Graded-Index Multimode Fibers," Photonics Technology Letters, IEEE, vol. 22, pp. 1708-1710, 2010.

(29) Y. Zhang, Y. Li, T. Wei, X. Lan, Y. Huang, G. Chen, and H. Xiao, "Fringe Visibility Enhanced Extrinsic Fabry-Perot Interferometer Using a Graded Index Fiber Collimator," Photonics Journal, IEEE, vol. 2, pp. 469-481, 2010.

(30) A. D. Yablon, Optical fiber fusion splicing. Berlin; New York: Springer, 2005.

(31) P. R. Horche, M. Lopez-Amo, M. A. Muriel, and J. A. Martin-Pereda, "Spectral behavior of a low-cost all-fiber component based on untapered multifiber unions," Photonics Technology Letters, IEEE, vol. 1, pp. 184-187, 1989

(32) M Hadjiprocopiou et. al., “Optimization of fibre coating properties for fiber optic smart structures” Smart Mater. Struct. vol. 5 pp.441, 1996

(33) E.J. Friebele, M.A. Putnam, and C.G. Askins, "Method for recoating optical fibres with polyimide," Electronics Letters , vol.34, no.12, pp.1249-1250, 11 Jun 1998

(34) E. Rivera, D. J. Thomson and A. A. Mufti, "Comparison of recoated fiber Bragg grating sensors under tension on a steel coupon", Proc. SPIE, 5767, 163 (2005)

(35) Andrew J. Tarpey, Stephen N. Kukureka and Kerstin Jurkschat, "Mechanical reliability of stripped and recoated polyimide fibers for optical fiber sensors", Proc. SPIE, 4639, 141 (2002)